NUCLEAR MATTER PROPERTIES USING CHIRAL INTERACTIONS UP TO FOURTH ORDER OF CHIRAL EXPANSION BASED ON PAULI OPERATOR

Khaled S.A. Hassaneen[†], Ahmed Refaat, Mohamed El-Zohary Ahmed Youssef[‡]

Physics Department, Faculty of Science, Sohag University
82524-Sohag, Egypt

Received 14 March 2024, accepted 15 July 2024, published online 2 August 2024

Using an expanded Brueckner–Hartree–Fock (BHF) framework with a phenomenological three-body force (3BF), we study the microscopic characteristics and equation of state (EOS) of symmetric nuclear and neutron matter. Both symmetric nuclear and pure neutron matter are used in the G-matrix computations, which are carried out by adding the 3BF to the initial two-body force (2BF) and employing a partial wave expansion. Using an angle-average and accurate Pauli operator, the single-particle potential is applied in both its standard and continuous forms. The fourth-order charge-dependent chiral nucleon–nucleon contact of the N3LO potential was used for the computations, both with and without the three-nucleon Urbana interaction included. It was found that the BHF approximation significantly improves the computations for symmetric nuclear matter at high density when one uses only the N3LO potential. As a matter of fact, it is shown that the 3BF is required for reproducing the empirical saturation property of symmetric nuclear matter in a non-relativistic microscopic framework and significantly alters the EOS of nuclear matter at huge densities above the typical nuclear matter density. A crucial component of the estimated equation of state of isospin-asymmetric nuclear matter is the nuclear symmetry energy. It establishes the structure of neutron stars and finite nuclei.

DOI:10.5506/APhysPolB.55.7-A3

1. Introduction

The equation of state (EOS) of nuclear matter is of great importance in nuclear physics and astrophysics [1–3]. The investigation of the EOS has been carried out using various methods [4]. Various approaches have been

[†] khaled.hassaneen@science.sohag.edu.eg
[‡] a.youssef1968@gmail.com

developed to study the short-range correlations and momentum distribution of nucleons in nuclear matter, such as the Bruckner–Hartree–Fock (BHF) approach. The BHF approach is one of the standard methods for infinite nuclear matter and has been used and developed in many studies. It is based on the solution of the two-nucleon equation in the nuclear medium and leads to an energy- and density-dependent effective interaction, the so-called G-matrix. For symmetric nuclear matter (SNM) and pure neutron matter (PNM), we have performed our calculations within the BHF approach in six cases. In three cases, we use the angular mean approximation of the Pauli operator with the continuous choice of the one-particle potential at different values of the momentum-space cut-off $\Lambda = 450$, 500, and 550 MeV, while in the other three cases, the conventional approximation with the same values of the momentum-space cut-off is used [5].

The calculations of the BHF approach depend on the choice of the single-particle potential [6], with the conventional choice assuming a single-particle energy of zero above the Fermi level [7], while the continuous choice assumes that the self-consistent BHF potential extends beyond the Fermi level. In this work, the next-to-next-to-next-to-leading-order (N3LO) potential [8] is used. The many-body method used to derive the EOS is a rather simple method, namely the non-relativistic BHF method with a conventional and continuous single-particle spectrum using the N3LO potential.

The chiral N3LO potential is a non-local potential and cannot be correctly described by a function of distance alone, but we must use a relative momentum between the nucleons to describe it. This potential is a high-precision phenomenological potential, there is a fourth-order nucleon–nucleon (NN) potential of the chiral perturbation theory. The accuracy in reproducing the NN data below 290 MeV laboratory energy is comparable to that of high-precision phenomenological potentials. Since NN potentials of order three and below are known to be quantitatively insufficient, the fourth order is necessary and sufficient for a reliable NN potential up to 290 MeV. The chiral N3LO potential consists of one-, two-, and three-pion exchanges and a series of contact interactions with zero, two, and four derivatives. The chiral N3LO potential proves to be as accurate as the Argonne V18 potential [9] in describing experimental data.

Since the early days of nuclear physics, it has been known that the EOS of nuclear matter contains a symmetry energy term. However, due to the development of radioactive ion-beam facilities, which allow one to study the structure and reactions of neutron-rich nuclei, in which the symmetry energy plays an important role, the experimental and theoretical study of the symmetry energy and its density dependence is becoming an increasingly interesting topic [10]. Finding the precise shape of the nuclear symmetry energy's density dependence is a significant and fascinating topic in both nuclear and astro-nuclear physics.

The dynamics of heavy-ion reactions [11], the neutron skin of nuclear systems, the structure of ground-state nuclei [12, 13], the physics of giant collective excitations [14], the physics of neutron stars [15], the structure of ground-state nuclei, the structure of nuclei near the drip line, and many other significant nuclear properties are all influenced by the symmetry energy. The symmetry energy, in particular its density dependence, has a major influence on the properties of neutron stars [16–18], hence its experimental and theoretical determination is very relevant and important. Since the symmetry energy is not a quantity that can be measured directly in experiments, it must be indirectly inferred from related observables.

The system's loss of binding energy upon moving from SNM to PNM is explained by the symmetry energy. The EOS of SNM and pure neutron matter were computed in the current work. Afterwards, the symmetry energy and incompressibility are calculated. The primary goal of this work is to discuss how the properties of nuclear matter are affected when the momentum-space cut-off value is revised.

2. Brueckner–Hartree–Fock

We have defined the G-matrix by

$$G(\omega) = V + V\frac{Q}{\omega - H_0 + i\eta}G(\omega)\,. \tag{1}$$

This is known as the Bethe–Goldstone equation, where ω is the initial energy, which is normally the sum of the single-particle energies of the states of the interacting nucleons

$$\omega = e(k) + e\left(k'\right)\,, \tag{2}$$

V is the bare NN potential, η is an infinitesimally small number, H_0 is the unperturbed energy of the intermediate scattering states, and Q is the Pauli projection operator. It projects out states with two nucleons above the Fermi level and is given by

$$Q\left(k,k'\right) = \left(1 - \Theta_{\mathrm{F}}(k)\right)\left(1 - \Theta_{\mathrm{F}}\left(k'\right)\right)\,, \tag{3}$$

where $\Theta_{\mathrm{F}}(k) = 1$ for $k < k_{\mathrm{F}}$ and zero otherwise, $\Theta_{\mathrm{F}}(k)$ is the occupation probability of a free Fermi gas with a Fermi momentum k_{F}. In the Brueckner–Goldstone expansion, the average binding energy per nucleon is expanded in a series of terms as following:

$$E(k)/A = \left\langle \hat{T} \right\rangle + \left\langle \hat{G} \right\rangle = \sum_k \frac{k^2}{2m} + \frac{1}{2}\sum_{k,k'<k_{\mathrm{F}}} \left\langle kk' \middle| G\left(e(k) + e\left(k'\right)\right) \middle| kk' \right\rangle\,, \tag{4}$$

where $|kk'\rangle$ refers to antisymmetric two-body states. This first order is called the Brueckner–Hartree–Fock (BHF) approximation. To fully determine the average binding energy, one must define the single-particle potential $U(k)$ that contributes to the single-particle energies that appear in the G-matrix elements. The structure of expression (4) suggests that the following BHF single-particle potential should be chosen:

$$U(k) = \sum_{k'<k_{\mathrm{F}}} \left\langle kk' \right| G\left(e(k) + e\left(k'\right)\right) \left|kk'\right\rangle , \tag{5}$$

so that

$$\begin{aligned} E(k)/A &= \sum_{k<k_{\mathrm{F}}} \left\{ \frac{k^2}{2m} + \frac{1}{2}U(k) \right\} \\ &= \frac{4}{\rho}\frac{1}{2}\int_0^{k_{\mathrm{F}}} \frac{4\pi k^2}{(2\pi)^3}\left(\frac{k^2}{2m} + e(k)\right) \mathrm{d}k \\ &= T_{\mathrm{F}} + \frac{3}{2k_{\mathrm{F}}^3}\int_0^{k_{\mathrm{F}}} k^2 \mathrm{d}k U(k)\,, \end{aligned} \tag{6}$$

where $T_{\mathrm{F}} = \frac{3k_{\mathrm{F}}^2}{10m}$.

The special choice (5) for $U(k)$ is also favourable because it leads to the cancellation of a certain higher-order diagram and thus improves the convergence of the hole line expansion [19]. One still has a self-consistent problem since the G-matrix itself depends on $U(k)$ through the initial energy ω defined in equation (2). The lowest-order approximation (4) together with the choice (5) for the single-particle potential is often referred to as the lowest-order Brueckner theory.

The single-particle energy $e(k)$ is defined as

$$e(k) = T + U(k) = \frac{\hbar^2 k^2}{2m} + U(k)\,, \tag{7}$$

where T is the kinetic energy. The conventional choice for the single-particle potential is the BHF potential (Eq. (5)) for hole states ($k < k_{\mathrm{F}}$) and zero for particle states ($k > k_{\mathrm{F}}$)

$$U(k) = \sum_{k'<k_{\mathrm{F}}} \left\langle kk' \right| G\left(e(k) + e\left(k'\right)\right) \left|kk'\right\rangle , \qquad k < k_{\mathrm{F}}\,, \tag{8}$$

$$U(k) = 0\,, \qquad k > k_{\mathrm{F}} \tag{9}$$

and thus introduces a rather large discontinuity in the spectrum of the individual particles on the Fermi surface. However, due to the unphysical discontinuity at the Fermi surface, this auxiliary potential cannot be directly related to the average potential of a particle or a hole.

Moreover, many other interesting properties can be derived, such as the momentum distribution and the effective mass, which are correctly described with a continuous spectrum at the Fermi surface. This was the main motivation that led Mahaux and his collaborators [20, 21] to introduce the continuous choice for the single-particle potential, treating particles and holes in a symmetric way. The use of the continuous potential implies that the elements of the G-matrix needed for the self-consistent calculation are complex, and the prescription recommended by Mahaux is

$$U(k) = \mathrm{Re} \sum_{k'<k_\mathrm{F}} \left\langle kk' \right| G\left(e(k) + e\left(k'\right)\right) \left| kk' \right\rangle \qquad \forall \ k\,. \tag{10}$$

Equations (1) and (7) are the most important equations that we want to solve self-consistently.

3. Three-body forces corrections

It is commonly known that the BHF technique is unable to accurately forecast the saturation properties of nuclear matter. Specifically, it has not been able to replicate both the saturation Fermi momentum ($k_\mathrm{F}^\mathrm{sat} = 1.36 \pm 0.05$ fm^{-1}) and the binding energy per nucleon ($e_0 = -16 \pm 1$ MeV) at the same time [6]. Results of different BHF computations for nuclear matter, when plotted on an energy-density plane, always lie roughly on a band, the Coester band [22], which considerably misses the "empirical box" for e_0 and $k_\mathrm{F}^\mathrm{sat}$. Due to this, using non-relativistic computations that incorporate contributions from phenomenological three-body forces (3BF) has grown in popularity.

3.1. Microscopic three-body force

As we see, non-relativistic calculations based on pure two-body interactions fail to reproduce the correct saturation point for SNM. This known deficiency is usually corrected by introducing the 3BF. Significant progress has been made in the theory of 3BF for nucleons, but a complete theory is not yet available. A realistic model for nuclear 3BF has been presented by the Urbana group [23]. Explicitly, the 3BF is written as the sum of two terms

$$V_{ijk} = V_{ijk}^{2\pi} + V_{ijk}^{\mathrm{R}}\,. \tag{11}$$

The first is an attractive term, $V_{ijk}^{2\pi}$, which is due to the exchange of two pions with the excitation of an intermediate resonance, Δ, while the second is a repulsive phenomenological central term V_{ijk}^{R}. The contribution of the two-pion exchange is a cyclic sum over the nucleon indices i, j, k of the products of anticommutator $\{,\}$ and commutator $[,]$ terms

$$V_{ijk}^{2\pi} = A \sum_{\mathrm{cyc}} \left(\{X_{ij}, X_{jk}\} \{\tau_i \cdot \tau_j, \tau_j \cdot \tau_k\} + \frac{1}{4} [X_{ij}, X_{jk}][\tau_i \cdot \tau_j, \tau_j \cdot \tau_k] \right) , \tag{12}$$

where

$$X_{ij} = Y(r_{ij}) \sigma_i \cdot \sigma_j + T(r_{ij}) S_{ij} \tag{13}$$

is the one-pion exchange operator, σ and τ are the Pauli spin and isospin operators, and

$$S_{ij} = 3 \left[(\sigma_i \cdot r_{ij})(\sigma_j \cdot r_{ij}) - \sigma_i \sigma_j \right]$$

is the tensor operator. $Y(r)$ and $T(r)$ are the Yukawa and tensor functions, respectively, associated with the one-pion exchange, as in the two-body potential. The repulsive part is assumed to be

$$V_{ijk}^{\mathrm{R}} = U \sum_{\mathrm{cyc}} T^2(r_{ij}) T^2(r_{jk}) \, . \tag{14}$$

The constants A and U in the previous equations can be adjusted to reproduce observed nuclear properties [24]. Moreover, the 3BF has been reduced to a two-body density-dependent force by averaging over the third nucleon in the medium [25].

These enter at two levels when 3BF are taken into account in BHF computations. Initially, a conventional G-matrix computation is performed, adding a density-dependent effective two-body interaction to the bare NN interaction. Furthermore, in order to prevent double counting of the 3BF contribution, the total energy must be rectified [26, 27]. This can be accomplished at the lowest order by deducting the Hartree–Fock contribution produced forth by 3BF alone [28]

$$\frac{E_{3\mathrm{BF}}}{A} = \frac{E_{2\mathrm{BF}}}{A} - \frac{1}{12} \frac{3}{k_{\mathrm{F}}^3} \int_0^{k_{\mathrm{F}}} k^2 \mathrm{d}k \, , \Sigma_{\mathrm{HF}}^{3\mathrm{BF}}(k) \, . \tag{15}$$

We emphasize that, in accordance with the methodology described in Ref. [26], the Hartree–Fock self-energy $\Sigma_{\mathrm{HF}}^{3\mathrm{BF}}$ originating from the 3BF is computed from an effective two-nucleon potential at the lowest order.

3.2. Phenomenological three-body force

There is another method to achieve saturation properties in nuclear matter. One should supplement the effective interaction or the self-energy of the BHF calculations with a simple contact interaction (CT), which we have chosen based on the notation of the Skyrme interaction and which has the form [29]

$$\Delta\mathcal{H} = \frac{3}{8}t_0\rho^2 + \frac{3}{48}t_3\rho^{2+\alpha}\,, \tag{16}$$

where ρ is the density of matter, t_0, t_3, and α are parameters. The exponent α controls the behaviour at high density, whereas the parameters t_0 and t_3 indicate the zero range and the 3-body strength. The contact term (CT) in the final equation has a Hamiltonian density that is independent of isospin. With various realistic NN interactions based on different values of α, the thermodynamic variables in symmetric nuclear matter have been explored using the BHF technique with CT [30].

3.3. Dirac correction

Ainsworth *et al.* [31] proposed corrections based on relativistic and other many-body effects. The lowest-order relativistic correction of the binding energy per nucleon can be derived from the modification of the self-energy of the scalar meson in nuclear matter and can be approximated as follows:

$$\left(\frac{E}{A}\right)_{\text{rel}} \propto \left(\frac{\rho}{\rho_0}\right)^{8/3} \text{MeV}\,. \tag{17}$$

This correction provides the saturating mechanism missing in the conventional Brueckner–Hartree–Fock calculations.

3.4. Chiral three-body forces

Carbone *et al.* [27] have studied symmetric nuclear matter with chiral two- and three-nucleon forces in both the BHF and self-consistent Green's functions. They proposed corrections due to the effects of chiral three-nucleon forces for the EOS of nuclear matter. These effects can be largely explained by the CT and its contribution to the total energy, which is proportional to C_{E}. In the Hartree–Fock approximation this is

$$\left(\frac{E_{C_{\text{E}}}}{A}\right)_{\text{chiral}} = -5.5\; C_{\text{E}} \left(\frac{\rho}{\rho_0}\right)^2 . \tag{18}$$

It is, therefore, expected that negative values of C_{E} [32] lead to more repulsive contributions to the EOS of nuclear matter. Then the saturation

point is close to the empirical value if its value corresponds to the interval $-0.660 \leq C_{\mathrm{E}} \leq -0.189$, where C_{E} expresses the strength of the CT of the three-nucleon interaction [33–35].

4. Results and discussion

4.1. The single-particle potential

The results of the single-particle potential calculation, which was done using Eq. (7), are shown in this section. At every stage of the iteration process, the quadratic approximation is introduced by fitting the potential up to a specific maximum momentum, denoted k_{fit}. The single-particle potential $U(k)$, obtained directly from the G-matrix calculation in Eq. (9), is fitted with a parabola at each iteration step and serves as the entry potential for the subsequent iteration. When both potentials under this approach stay stable, convergence is obtained.

Figure 1 uses the N3LO potential at different values of the momentum-space cut-off $\Lambda = 450$ (first panel), 500 (second panel), and 550 MeV (third panel), for three different values of densities, to illustrate the dependence of the single-particle potential on the momentum k up to $k_{\mathrm{fit}} = 1.5\,k_{\mathrm{F}}$ for SNM. These are $\rho = 0.5\,\rho_0$, ρ_0, and $2\,\rho_0$ in terms of the Fermi momentum k_{F}, where ρ_0 is the saturation density $\rho_0 = 0.17$ fm^{-3}. As is the case for SNM, the Fermi momentum k_{F} is connected to the total baryon number density using the formula $\rho = 2k_{\mathrm{F}}^3/(3\pi^2)$. The solid line indicates continuous choice, while the dashed line indicates traditional choice. We note that above k_{F}, the single-particle potential resulting in the conventional choice at high momentum k vanishes. This indicates that for values higher than the Fermi momentum k_{F}, the potential's effect vanishes. In contrast, the continuous choice shows that the potentials are more attractive and that their influence extends even at high momentum k; this indicates that the potential's effect continues for values higher than the Fermi momentum k_{F}. This is in line with the research presented in Ref. [36], which indicates that the correlation energy tends to increase when the gap at k_{F} in the single-particle potential is suppressed.

The single-particle potential in the BHF approach of pure neutron matter (PNM) is represented by chiral NN potentials for the three cases of the cut-off energy Λ of the N3LO interaction, as shown in Fig. 2. The curves show the results without the 3BF effects for three densities, $\rho = 0.5\rho_0$, ρ_0, and $2\rho_0$ in terms of the Fermi momentum k_{F}^n, where $\rho_0 = 0.17$ fm^{-3}. For the auxiliary potential for three different values of k_{F}^n, the dashed line represents the conventional choice and the solid line represents the continuous choice. The formula $\rho = (k_{\mathrm{F}}^n)^3/(3\pi^2)$ is used to relate the Fermi momentum of PNM k_{F}^n to the overall baryon number density.

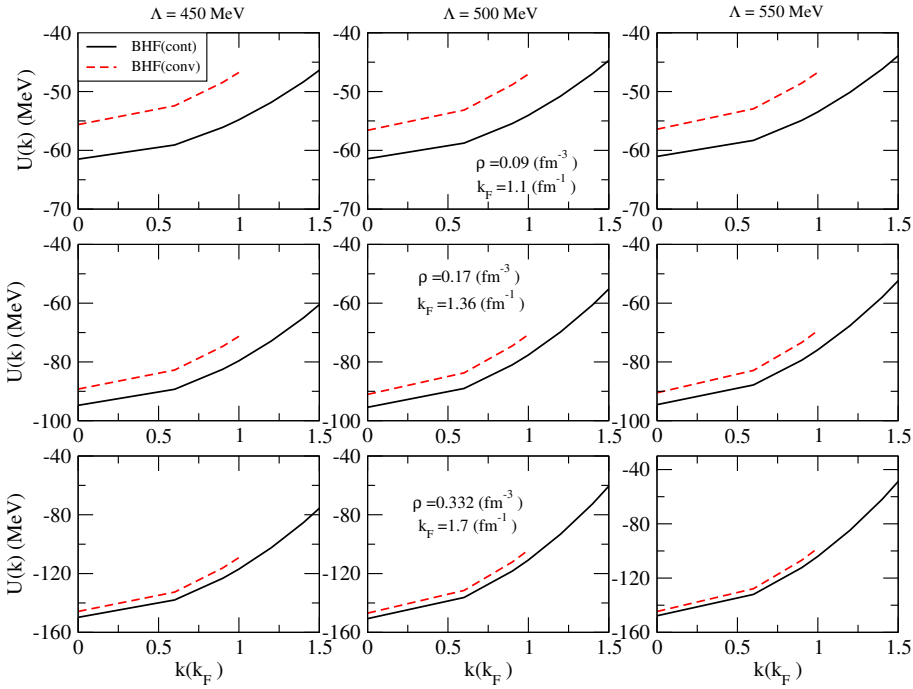

Fig. 1. The single-particle potential within the BHF approach of SNM using chiral NN potentials for the three instances of the cut-off energy Λ of the N3LO interaction. The curves show the results without the 3BF effects at three values of densities: $\rho = 0.5\rho_0$, ρ_0, and $2\rho_0$ in terms of the Fermi momentum $k_{\rm F}$, where $\rho_0 = 0.17$ fm^{-3}. The dashed curve represents the results with conventional choice, whereas the solid line shows the continuous choice for the auxiliary potential at three different values of $k_{\rm F}$.

It is evident from figures 1 and 2 that the high-momentum BHF single-particle potential, which has been shown to be too attractive at high densities and whose momentum dependence turns out to be too weak to describe the experimental elliptic flow data in heavy-ion collisions (HIC) at high energies, cannot be significantly improved by correlations induced by the two-body force (2BF) alone [37, 38]. To enhance the single-particle potential's high-momentum behaviour in the Brueckner theory, the 3BF effect must be taken into account.

We next compare the single-particle potentials, or the real part of the on-shell self-energies in SNM (left panel) and PNM (right panel) in Fig. 3 in order to clearly understand the 3BF effects. The N3LO potential with a momentum-space cut-off of $\Lambda = 500$ MeV and an exact treatment of the Pauli operator is used in these computations as suggested by Schiller *et al.* [39].

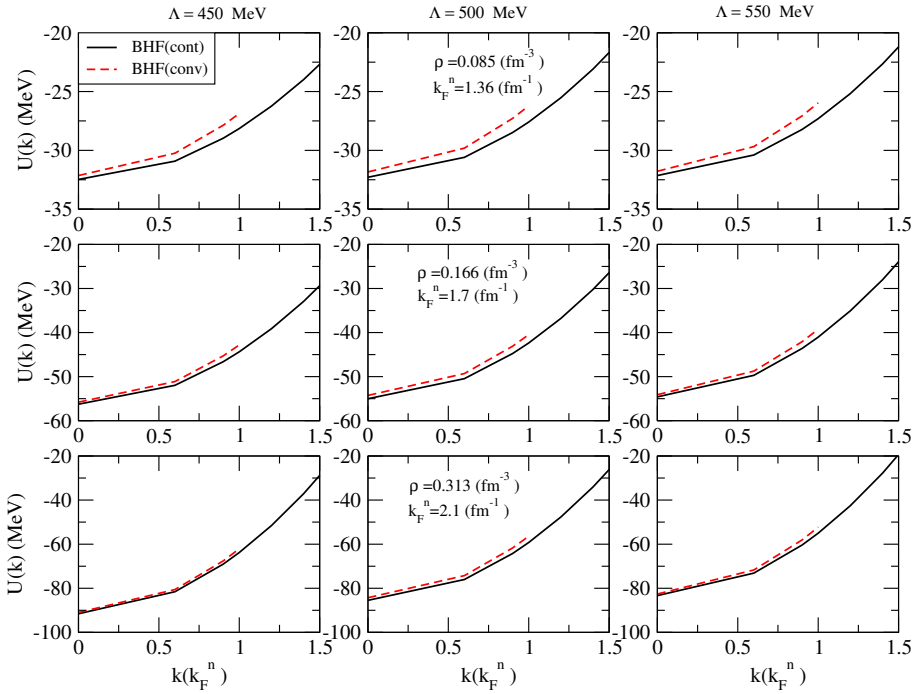

Fig. 2. The single-particle potential within the BHF approach of PNM using chiral NN potentials with three different cut-off values. The dashed curve represents the results with conventional choice, whereas the solid line shows the continuous choice for the auxiliary potential at three different values of $k_{\rm F}^n$.

The results for both approaches are obtained at three distinct densities: 0.09, 0.17, and 0.33 fm^{-3}. It can be seen that the single-particle potential is most attractive at the BHF level (solid curves) without the inclusion of 3BF. At low densities below and close to the normal nuclear matter density, the 3BF effects (red dashed curves) are quite small. The 3BF effects quickly become significant with the increasing density. In particular, the depth of the potential, *i.e.* $U_0(k=0)$, decreases from -60.2 to -59.6 MeV at $\rho = 0.09$ fm^{-3}, while at the normal density ρ_0, *i.e.* at $\rho = 0.17$ fm^{-3}, it starts at -94.9 and decreases to -90.2 MeV. This difference increases at high density, where the depth has the value of -146.9 MeV and becomes -116.8 MeV when the 3BF are included in the BHF approach at density of $\rho = 0.33$ fm^{-3}. This means that in the context of the Brueckner theory, the 3BF affects the predicted single-particle potentials or self-energies in two different ways: First, it affects the self-energies at the BHF and extended BHF levels directly via its modification of the G-matrix.

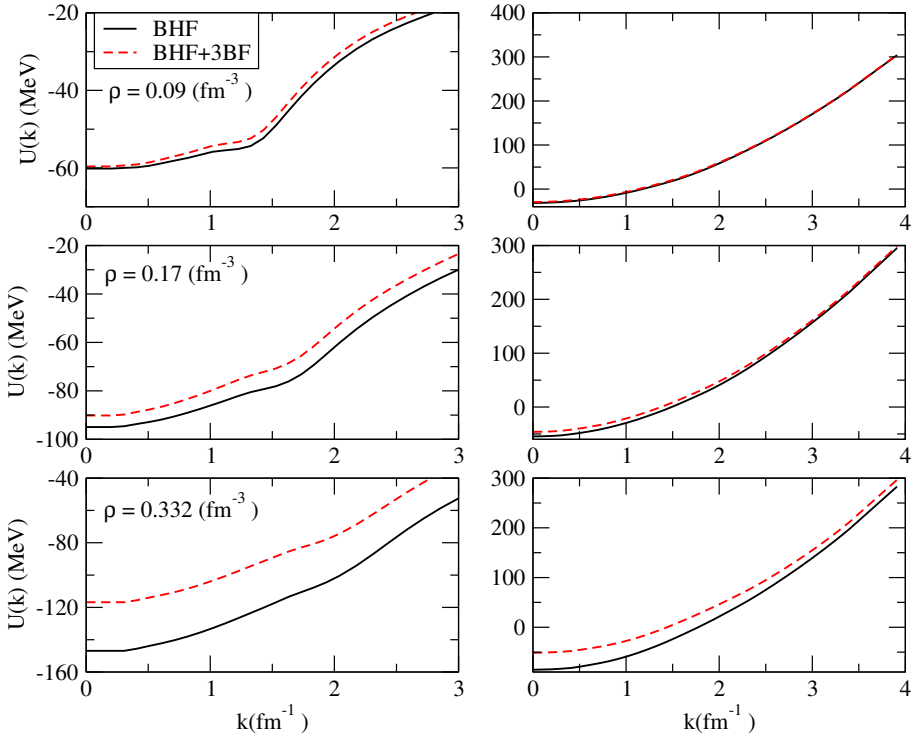

Fig. 3. At momentum-space cut-off values of $\Lambda = 500$ MeV, the single-particle potential as a function of momentum k within the BHF method of SNM (left panel) and PNM (right panel) employing the chiral N3LO potential with and without incorporating 3BF. The dashed line displays BHF with the 3BF included and an exact Pauli operator for the auxiliary potential at three distinct densities ρ, whereas the solid curve displays the BHF results.

Accordingly, $U(k) = U_{\rm BHF}(k) + U_{\rm 3BF}(k)$ represents the entire single-particle potential, where $U_{\rm BHF}(k)$ denotes the lowest-order BHF single-particle potential and $U_{\rm 3BF}(k)$ represents the contribution caused by the 3BF. Moreover, particularly at high densities, it can play a significant role as a repulsion to the single-particle potential. Eventually, we can say that the 3BF effect lowers the momentum dependence of the single-particle potential and offers a small amount of repulsion at high densities through its modification of the G-matrix at the BHF level. This repulsion is more noticeable at lower momenta.

More specifically, all these single-particle potentials exhibit significant deviation from a parabolic shape at momenta somewhat above the Fermi momentum. In analysing the self-energy for particle states using Eq. (10), it is evident that such a divergence tends to yield more appealing matrix

elements of G, which results in greater binding energy. This result is consistent with what the earlier studies [40, 41] have shown. In addition, as expected, the 3BF adds a repulsive contribution to the single-particle potentials. This repulsion in the effective three-body interaction may be induced by the effects of sub-nucleonic degrees of freedom, like, *e.g.*, the many-body effects arising from Δ excitations of the nucleons [23, 42]. Therefore, it has been demonstrated in Refs. [43, 44] that this strongly repulsive and momentum-dependent contribution caused by the 3BF is essential to minimizing the discrepancy between the high-momentum and large-density BHF single-particle potential in symmetric matter and the parametrized potential for characterizing elliptic flow data [37] and those anticipated by the Dirac Brueckner–Hartree–Fock approach [45].

The single-particle potential values in SNM at low momenta are more attractive than those in pure neutron matter, as can be shown by comparing figures 1, 2, and 3. This is because the absence of the ${}^3S_1$–${}^3D_1$ increases the attraction. However, at high momenta, the SNM's single-particle potential values are more repulsive than those of PNM. The values of the potential depth, which translate into the value of $U(k)$ at $k = 0$ for both SNM and PNM, are listed in Table 1. We observe that when density increases, the potential depth falls. Furthermore, compared to the exact Pauli operator, it is more repulsive in the angle average approximation. This is due to the fact that, in the exact Pauli operator, the effective interaction between nucleons is more attractive than in the angle average approximation [6]. The values of the single-particle potential get more repulsive at high momentum and more attractive at low momentum as the density increases. Furthermore, the curves converge from each other when the values for the continuous choice and the conventional one differ less, whereas the curves diverge when the values for the angle average estimate and the exact Pauli operator differ more.

4.2. The nuclear matter binding energy (E/A)

Figure 4 displays the outcomes of our non-relativistic BHF computations using an N3LO potential and varying momentum-space cut-off values of $\Lambda = 450$, 500, and 550 MeV. The E/A of SNM is shown in the left panel, while the E/A of PNM is shown in the right panel as a function of the Fermi momentum k_{F} in fm^{-1}. Conventional choice is represented by the dashed line; continuous choice is represented by the solid line. The empirical saturation one is indicated by the large square box.

One observes from the figure that the binding energy per nucleon first decreases with increasing k_{F}, until it reaches the minimum (saturation) point then it increases with increasing k_{F}. The continuous choice leads to an

Table 1. The values of the single-particle potential, depth, at $k = 0$, determined by the BHF approach using an N3LO potential with variable momentum cut-off. For the single-particle potential at three different density values in the case of symmetric and pure nuclear matter, these values are calculated both by convention and by continuous choice. In addition, the depths in the case of BHF with and without the inclusion of 3BF are calculated for symmetric and pure nuclear matter with an exact treatment of the Pauli operator.

N3LO	U_0 at $k = 0$	for SNM	(conv. choice)
cut-off	$\rho = 0.5\rho_0$	$\rho = \rho_0$	$\rho = 2.0\rho_0$
$\Lambda = 450$	-55.6155	-89.2249	-145.7923
$\Lambda = 500$	-56.5818	-91.0449	-146.9366
$\Lambda = 550$	-56.4083	-90.5053	-144.6329
	U_0 at $k = 0$	for SNM	(cont. choice)
$\Lambda = 450$	-61.4997	-94.7601	-149.801
$\Lambda = 500$	-61.4333	-95.4183	-150.6668
$\Lambda = 550$	-61.0362	-94.5299	-147.7915
	U_0 at $k = 0$	for PNM	(conv. choice)
$\Lambda = 450$	-32.1465	-55.7878	-91.0035
$\Lambda = 500$	-31.8367	-54.256	-84.305
$\Lambda = 550$	-31.781	-54.089	-82.6307
	U_0 at $k = 0$	for PNM	(cont. choice)
$\Lambda = 450$	-32.4785	-56.2524	-91.5634
$\Lambda = 500$	-32.2888	-55.0108	-85.4816
$\Lambda = 550$	-32.1429	-54.5824	-83.3349
N3LO (BHF)	U_0 at $k = 0$	for SNM	(exact Pauli)
$\Lambda = 500$	-60.1684	-94.9291	-146.8735
N3LO BHF+3BF	U_0 at $k = 0$	for SNM	(exact Pauli)
$\Lambda = 500$	-59.6098	-90.1675	-116.79225
N3LO (BHF)	U_0 at $k = 0$	for PNM	(exact Pauli)
$\Lambda = 500$	-31.4133	-54.5048	-85.3181
N3LO BHF+3BF	U_0 at $k = 0$	for PNM	(exact Pauli)
$\Lambda = 500$	-29.3735	-46.0399	-51.3033

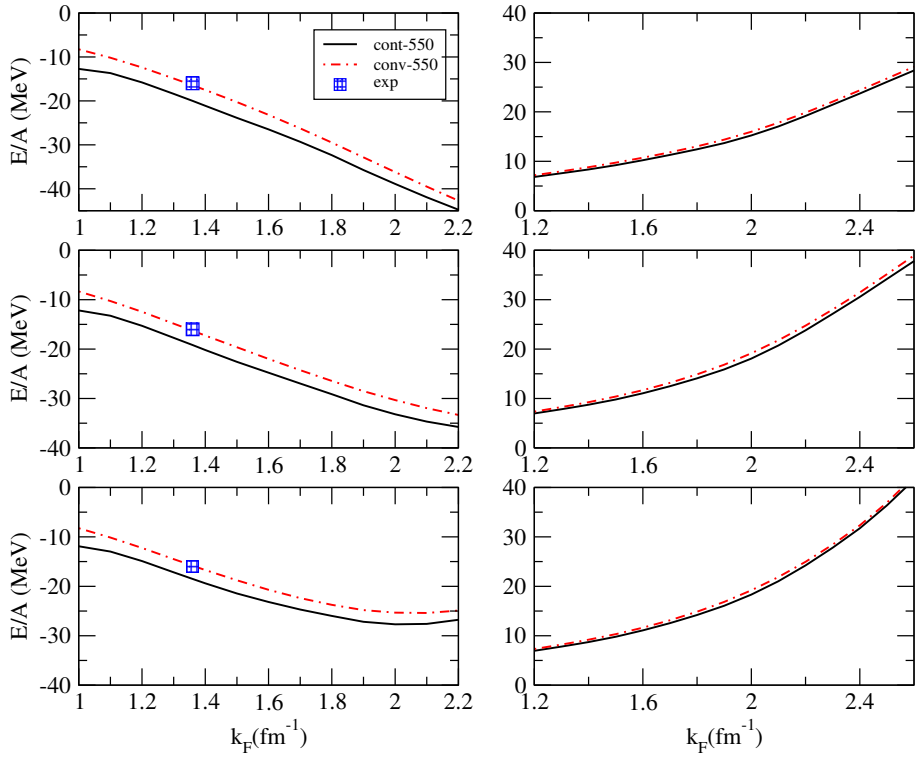

Fig. 4. The binding energy per nucleon (E/A) calculated for SNM as a function of the Fermi momentum within the BHF approach using the chiral N3LO potential with three values of momentum-space cut-off values of Λ. The dashed line represents the results with conventional choice, whereas the solid one with the continuous choice for the auxiliary potential. The large square indicates the empirical saturation area.

enhancement of correlation effects in the medium and tends to predict larger binding energies for nuclear matter than the conventional choice. What we observe in the present calculation is that in the continuous choice, the energy per particle becomes more and more repulsive with increasing the Fermi momentum k_{F}. As predicted, the two-body BHF calculation exhibits excessive attraction and it is impossible to obtain saturation up to very high density, especially when chiral N3LO potentials with variable momentum-space cut-off values of $\Lambda = 450$, 500, and 550 MeV are used. As a result, the non-relativistic BHF is unable to produce the saturation property's density or magnitude close to the empirical estimations (shown as rectangles) using just 2BF.

Plotting the energy per particle E/A against the Fermi momentum k_{F} for PNM using various potentials is shown in the right panel of Fig. 4. The solid line represents the continuous choice, while the dashed line represents the conventional choice. The figure shows that, in accordance with most many-body computations, the EOS of the PNM is unbound, with the energy per nucleon increasing roughly monotonically with the increasing Fermi momentum. We find that the differences between the two techniques are negligible because the $(T = 0)$ ${}^3S_1$–${}^3D_1$ coupled states mostly reflect the strength of the tensor force, which is the main cause of the differences between the potentials. That partial wave, however, is not present in PNM $(T = 1)$.

4.3. Inclusion of 3BF in the BHF approach and its effect in EOS

It is generally known that the empirical saturation point of SNM cannot be reproduced using two-body nuclear interactions alone, even in the most advanced non-relativistic quantum many-body techniques. Actually, the saturation points found with the BHF approximation are limited to a small region known as the Coester band [22, 46], and they either have an excessively high saturation density in comparison to the empirical values. For the N3LO potential, the saturation density in the BHF approximation is $\rho_0 = 0.48$ fm^{-3} at $e_0 = -27.7$ MeV. This value is very different from the empirical value, which has $E/A_{\mathrm{exp}} = -16$ MeV and $\rho_0 = 0.17$ fm^{-3}. This can be fixed by using Chiral 3BF, Dirac correction, CT, or three-body forces.

Using the chiral N3LO interaction and the BHF approach discussed in the previous two sections, we present and discuss the results of our calculations for the equation of state, *i.e.*, the energy per particle E/A as a function of the Fermi momentum k_{F} for SNM. After precisely handling the Pauli operator and energy denominator, the partial waves of the Bethe–Goldstone Eq. (1) can be expanded. We have taken into account partial wave contributions in all of the computations done in this study, up to a total two-body angular momentum of $J_{\mathrm{max}} = 8$. The energy per particle of SNM for the interaction model under consideration is displayed in Fig. 5. The dashed lines in each panel denote calculations where the contribution of the 3BFs to the energy per nucleon was included, whereas the solid lines in each panel relate to calculations made using the two-body potential without any 3BF.

As Fig. 5 illustrates, the 3BF yield nuclear saturation points included at $e_0 = -16.86$ MeV are very close to the empirical estimates $\rho_0 = 0.2$ fm^{-3}. At the highest concentrations, the 3BF contribution may, nevertheless, be more than the 2BF contribution. The results of the EOSs employing the relativistic correction are more stiff than those obtained using BHF+3BF. Saturation points obtained by applying BHF+CT as the Skyrme force at

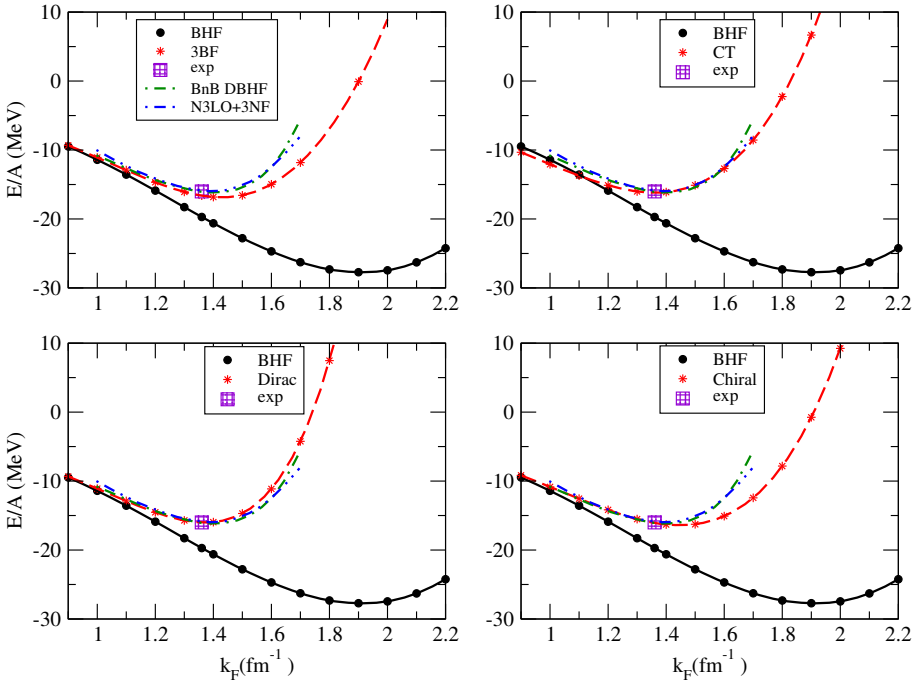

Fig. 5. The energy per particle (E/A) of SNM *versus* the Fermi momentum $k_{\rm F}$, within different models described in the text using the N3LO potential. The empirical saturation point is given by the large blue square. All results are compared with BnB DBHF (green) and N3LO+3NF (blue) EOS achieved by Sammarruca *et al.* [48].

value $\gamma = 0.5$ agree with the empirical value. The saturation threshold for chiral 3BF is thus quite near to the empirical values $\rho_0 = 0.21$ fm^{-3} at $e_0 = -16.41$ MeV with value of $C_{\rm E} = -0.65$. Up to a density of roughly 0.3 fm^{-3}, the comparison shows a good agreement; however, at greater densities, both the variational and relativistic calculations point to a stiffer trend. With the possible exception of the relativistic one, which, at higher densities, seems excessively repulsive. According to the analysis, the EOS must be somewhat soft at low densities. This has important implications for the stiffness of the resulting β-stable equation of state, in particular, for astrophysical applications such as the study of neutron stars structure [17, 47]. Table 2 contains the findings of the saturation point evaluations for both interaction models and all current SNM approaches.

Table 2. A summary of the key properties of nuclear matter that the equation of state at saturation points can be used to derive. The saturation density and energy are denoted by ρ_0 in fm^{-3} and $-e_0$ in MeV, respectively, and the incompressibility, symmetry energy, and slope parameter in MeV are denoted by K_0, E_{sym}, and L. The experimental values are displayed in the last column. Every result is computed using the BHF method, both with and without the 3BF, CT, Dirac correction, and chiral 3BF.

	BHF	3BF	Skyrme	Dirac	Chiral	Exp. ∼ [61]
ρ_0	0.48	0.20	0.17	0.174	0.21	0.14–0.17
$-e_0$	27.7	16.86	16.20	16.02	16.41	15–16
K_0	282.4	305.9	193.9	257.7	206.1	220–260
E_{sym}	60.5	33.27	30.77	34.64	35.67	28.5–34.9
L	121.8	64.55	45.28	74.55	63.85	30–87

Such calculations were performed early for the N3LO potential by Sammarruca *et al.* [48]. They have taken into consideration two very different approaches to the analysis of nucleonic matter: one based on chiral effective three-nucleon forces at NNLO and a N3LO potential, the other based on a meson-theoretic potential and the DBHF approximation. The nuclear EOS is among the predictions that they have taken into account. The results of their approaches are shown in Fig. 5 with BnB DBHF (green) and N3LO+3NF (blue) EOS. The results they obtained demonstrate that the DBHF approach is a great phenomenology that can include significant many-body effects, which are essential for nuclear saturation. In both cases, a single nucleon interacting with the Fermi sea produces the effective 3NF. This indicates the complementarity of the two approaches to explaining nuclear forces. On the other hand, the proposed 3BF in the current computation significantly improves the expected saturation qualities and makes a repulsive contribution to the EOS of nuclear matter, but it is not as effective as chiral effective three-nucleon forces or DBHF, particularly at high densities. However, using equations (16) and (17), similar results can be obtained if Dirac or contact term corrections are included in BHF.

For a number of reasons, the EOS of neutron matter close to nuclear densities is significant. Since various channels have a significant role in the NN interaction in this regime — as previously mentioned — the EOS examines various frames for the nuclear Hamiltonian directly. The EOS dominates the maximum mass of neutron stars at very high densities, but the pressure in the region ~ 1–$2\rho_0$ determines their radius, which may be measured and utilized to constrain the EOS [49].

However, multiple *ab initio* calculations in neutron matter have shown the importance of 3BF, which lead to extra net repulsion and increase neutron matter's binding energy by several MeV at ρ_0. Figure 6 presents a comparison of the BHF (solid curve) with other *ab initio* calculations for the PNM, including both NN and 3BF. The dot-dashed BHF+Dirac curve, the dot-double-dashed BHF+3BF curve, the dashed BHF+CT curve, and the dash-double-dotted BHF+chiral curve are these methods. The most noticeable difference between Fig. 6 and BHF alone, as seen by the solid curve, is the repulsion between three-nucleon interactions in neutron matter. Furthermore, Dirac and chiral 3BF both strongly generate this repulsion in comparison to BHF with CT.

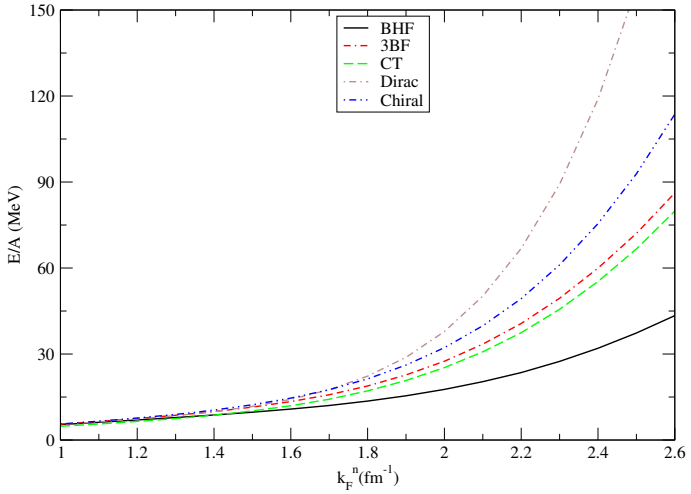

Fig. 6. The energy per particle (E/A) of pure neutron matter *versus* the Fermi momentum k_{F}^{n}, within different models described in the text using the N3LO potential.

4.4. Symmetry energy E_{sym} and slope parameter L

Combining the EOS of PNM and SNM gives us insights into the isospin effects [50], specifically with the symmetry energy E_{sym}. As a second derivative of energy per nucleon E/A with regard to the asymmetry parameter α, the symmetry energy of nuclear matter is described as follows:

$$E_{\mathrm{sym}}(\rho) = \frac{1}{2}\left[\frac{\partial^2 E/A(\rho,\alpha)}{\partial\alpha^2}\right]_{\alpha=0}. \tag{19}$$

The simple α^2-law, $E_{\mathrm{sym}}\,\alpha^2 = E/A(\rho,\alpha) - E/A(\rho,0)$, is satisfied by the binding energy per nucleon E/A, as demonstrated by numerous studies

[51, 52]. This holds true not only for $\alpha \ll 1$, as assumed in the empirical nuclear mass formula [53], but also during the whole asymmetry range, with a linear behaviour. Two significant results follow from the α^2-law of the EOS of asymmetric nuclear matter (ANM) at any isospin asymmetry. Firstly, it shows that the symmetry energy and the EOS of SNM provide the whole EOS of ASM at any isospin asymmetry. Second, it suggests that the symmetry energy explicitly determines the difference between the chemical potentials of the neutron and proton in a β-stable neutron star: According to $\mu_n - \mu_p = 4\alpha\, E_{\rm sym}$ [52], the symmetry energy is essential for determining the make-up of neutron stars. By using the difference between the binding energies of SNM $E/A(\rho, \alpha = 0)$ and PNM $E/A(\rho, \alpha = 1)$, we may compute the symmetry energy $E_{\rm sym}$, *i.e.*,

$$E_{\rm sym}(\rho) = E/A(\rho, \alpha = 1) - E/A(\rho, \alpha = 0)\,, \tag{20}$$

however, using it at an extremely high density is not advised. Figure 7 illustrates the symmetry energy as a function of density ρ, in accordance with Eq. (20). Table 2 lists its values at saturation points for BHF, BHF+3BF, BHF+CT, BHF+chiral, and BHF+Dirac calculations, which are 60.5, 33.27, 30.77, 34.64, and 35.67 MeV, respectively. Table 2 illustrates how these values are in close vicinity to the empirical value range. This gap can be traced back to the contribution of correlations resulting from relativistic, chiral, or 3BF at all densities in SNM and PNM. When compared to BHF calculations, this leads to higher binding energies (see figures 5 and 6).

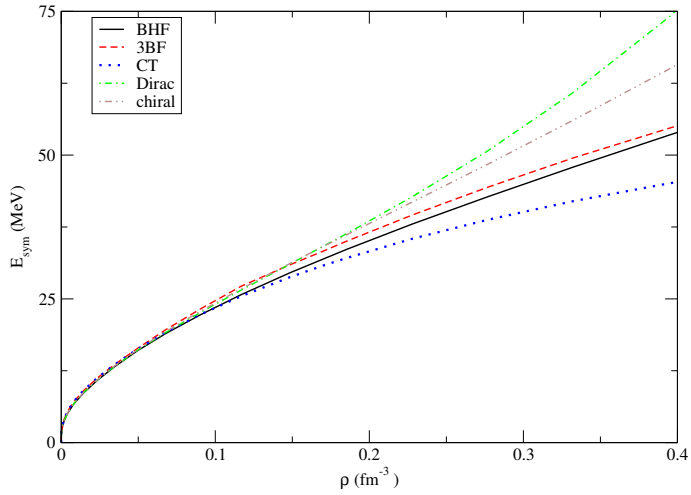

Fig. 7. The symmetry energy obtained as a function of the density ρ.

The minimum of $e_0(\rho) = E/A(\rho, \alpha = 0)$ at a density approximately equal to the average central density of nuclei, ρ_0, is a reflection of the saturating nature of the nuclear force. Next, we will expand the symmetry energy about the saturation point

$$E_{\rm sym}(\rho) \approx E_{\rm sym}(\rho_0) + L\frac{\rho - \rho_0}{3\rho_0} + \frac{K_{\rm sym}}{2}\frac{(\rho - \rho_0)^2}{(3\rho_0)^2}\,, \tag{21}$$

which helps identify several useful parameters. L is referred to as the slope parameter, as it is a measure of the slope of the symmetry energy at saturation

$$L = 3\rho_0 \left(\frac{\partial E_{\rm sym}(\rho)}{\partial \rho}\right)_{\rho_0}\,. \tag{22}$$

Furthermore, it is obvious from Eqs. (20) and (22) that L is a measure of the slope of the NM EOS at saturation density, since the SNM EOS has a vanishing slope at that point.

The parameter $K_{\rm sym}$ characterizes the curvature of the symmetry energy at saturation density

$$K_{\rm sym} = 9\rho_0^2 \left(\frac{\partial^2 E_{\rm sym}(\rho)}{\partial \rho^2}\right)_{\rho_0}\,. \tag{23}$$

Note that a similar expansion of the energy per particle in SNM identifies the quantity

$$K_0 = 9\rho_0^2 \left(\frac{\partial^2 e_0(\rho)}{\partial \rho^2}\right)_{\rho_0} \tag{24}$$

as a measure of the curvature of the EOS in SNM.

Using the standard thermodynamic relation,

$$P(\rho) = \rho^2 \frac{\partial e}{\partial \rho}\,, \tag{25}$$

where P is the pressure and e is the energy per particle, we define the symmetry pressure as

$$P_{\rm sym}(\rho) = \rho^2 \frac{\partial (e_n - e_0)}{\partial \rho} = P_{\rm NM}(\rho) - P_{\rm SNM}(\rho)\,. \tag{26}$$

Since the pressure in SNM disappears at saturation, the symmetry pressure is effectively the pressure in NM if the derivative is evaluated at or very near ρ_0. Then

$$P_{\rm NM}(\rho_0) = \left(\rho^2 \frac{\partial e_n(\rho)}{\partial \rho}\right)_{\rho_0}\,, \tag{27}$$

where $e_n = E/A(\rho, \alpha = 1)$. It is evident from equations (22) and (27) that the slope parameter L represents the pressure in NM around saturation density

$$P_{\mathrm{NM}}(\rho_0) = \rho_0 \frac{L}{3}, \tag{28}$$

demonstrating that, for normal density, the pressure in NM is proportional to the slope of the symmetry energy. The development and dimensions of the neutron skin are thus determined by the value of L, which is a measure of the pressure gradient forcing extra neutrons outward from the nucleus's neutron-enriched core to the outside region [54].

A few of our estimates for the slope parameter L using the current methods are displayed in Table 2. Chiral predictions typically have a softer aspect, as was already noted. Reference [55] provides a comparison with other phenomenological interactions, including Argonne V18 and the UIX 3NF [56]. Values for $E_{\mathrm{sym}}(\rho_0)$ and L are reported to be (31.7 ± 1.1) MeV and (59.8 ± 4.1) MeV, respectively, in a more recent analysis [57].

4.5. Pressure P and incompressibility K_0

Equation (25) defines the pressure of nuclear matter in terms of energy per nucleon. The pressure produced from the BHF, BHF+3BF, BHF+CT, BHF+Dirac, and BHF+chiral techniques based on EOS for symmetric matter is displayed in figure 8. The region enclosed by the closed lines suggests that EOS agrees with the elliptic flow measurements of SNM that were published in Ref. [58]. Two distinct parametrisations for the symmetry energy are considered in the analysis for the case of neutron matter. The two pressure contours shown in figure 9 represent the density dependence for $E_{\mathrm{sym}}(\rho)$ proposed by Prakash *et al.* [59], which are the weakest (lower contour with continuous line) and the strongest (upper contour with dotted line). It is plausible to conclude that, in comparison to Dirac calculations, which produce high pressure, BHF+CT and BHF+chiral predictions produce an acceptable level of repulsion; in contrast, BHF+3BF results produce a weakly repulsive EOS.

The incompressibility K of the EOS is another significant property that comes up when discussing a range of phenomena, including supernova explosions and heavy-ion collisions. It gauges the EOS's stiffness, which is often expressed as the pressure's saturation point slope, as provided by Eq. (24). It has been determined that the experimental value of the incompressibility at saturation density ρ_0 is 230 ± 40 MeV [60]. Table 2 summarizes the incompressibility values and other bulk parameters derived for SNM at the saturation density.

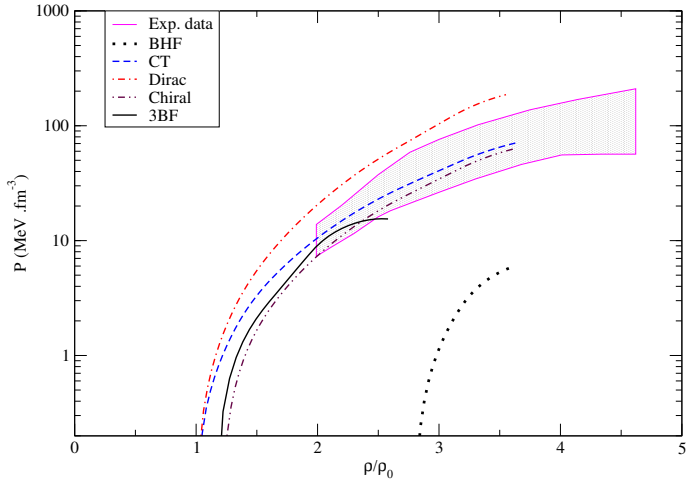

Fig. 8. The pressure in [MeV/fm^3] for SNM as a function of ρ/ρ_0 for different approaches using the N3LO potential. The area enclosed by the continuous line corresponds to the region of pressure consistent with the experimental data [58] for SNM.

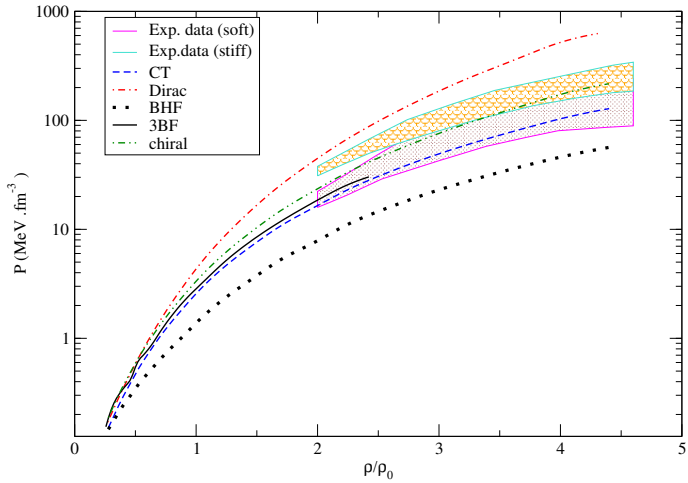

Fig. 9. The same as Fig. 8 but for PNM.

5. Conclusion

At the end of this study, it was investigated how sensitive the Brueckner–Hartree–Fock approximation is to an angle-averaged and exact treatment of the Pauli propagator in the Bethe–Goldstone equation for the many-particle

system of symmetric nuclear and PNM. In particle states involving three-body forces, one finds that the exact treatment of the Pauli operator in combination with a one-particle spectrum based on the real part of the self-energy leads to results: First, the 3BF correlations provide a repulsive contribution to the neutron and proton single-particle potentials and mainly change the single-particle properties at low momenta around and below the Fermi surfaces. Second, a result for the binding energy per nucleon that is not negligibly larger than the results obtained with standard approximation schemes.

Furthermore, we would like to note that the EOS is very sensitive to any change in the momentum space cut-off, especially at high densities. We find that the EOS of SNM exhibits a greater dependence on the momentum-space cut-off when compared to that of PNM. In the case of utilizing the angular mean approximation with its two options, increasing the momentum-space cut-off results in a gain; the EOS takes its proper shape and saturates at 550 MeV momentum-space cut-off. It is consistent with other research, nevertheless, the benefits of this gain are not very significant near the empirical saturation point. The evaluated model still lacks the proper binding energy per nucleon and symmetry energy values at saturation; hence, adjustments to the 3BF or Dirac contribution must be made to account for this problem.

The current methods utilizing chiral NN interactions predict a monotonically increasing symmetry energy as a function of density. The 3BF influence is quite weak on symmetry energy at the sub-saturation level. The relativistic and chiral components in both the BHF+Dirac and BHF+chiral approaches bend up the symmetry energy curve at suprasaturation densities, which causes a stiffening of the density dependence of symmetry energy. When it comes to symmetry energy, the BHF framework has far larger repulsive impact at high densities than the BHF+CT and BHF+3BF frameworks.

Khaled S.A. Hassaneen would like to express gratitude to R. Machleidt for giving us the chiral potentials and Marcello Baldo for providing us with the three-body force code. The authors also thank Professor Herbert Müther for his insightful talks and advice.

REFERENCES

[1] K.C. Chung, C.S. Wang, A.J. Santiago, J.W. Zhang, «Nuclear matter equation of state based on effective nucleon–nucleon interactions», *Phys. Rev. C* **61**, 047303 (2000).

[2] A. Peshier, B. Kämpfer, G. Soff, «Equation of state of deconfined matter at finite chemical potential in a quasiparticle description», *Phys. Rev. C* **61**, 045203 (2000).

[3] J. Margueron, E. van Dalen, C. Fuchs, «Low densities in asymmetric nuclear matter», *Phys. Rev. C* **76**, 034309 (2007).

[4] H. Müther, A. Polls, «Two-body correlations in nuclear systems», *Prog. Part. Nucl. Phys.* **45**, 243 (2000).

[5] D.R. Entem, R. Machleidt, Y. Nosyk, «High-quality two-nucleon potentials up to fifth order of the chiral expansion», *Phys. Rev. C* **96**, 024004 (2017).

[6] Kk.S.A. Hassaneen, H.M. Abo-Elsebaa, E.A. Sultan, H.M.M. Mansour, «Nuclear binding energy and symmetry energy of nuclear matter with modern nucleon–nucleon potentials», *Ann. Phys.* **326**, 566 (2011).

[7] H. Kümmel, K.H. Lührmann, J.G. Zabolitzky, «Many-fermion theory in expS- (or coupled cluster) form», *Phys. Rep.* **36**, 1 (1978).

[8] D.R. Entem, R. Machleidt, «Accurate charge-dependent nucleon–nucleon potential at fourth order of chiral perturbation theory», *Phys. Rev. C* **68**, 041001(R) (2003).

[9] R.B. Wiringa, V.G.J. Stoks, R. Schiavilla, «Accurate nucleon–nucleon potential with charge-independence breaking», *Phys. Rev. C* **51**, 38 (1995).

[10] I. Tanihata, «Neutron halo nuclei», *J. Phys. G: Nucl. Part. Phys.* **22**, 157 (1996).

[11] B.A. Li, L.W. Chen, C.M. Ko, «Recent progress and new challenges in isospin physics with heavy-ion reactions», *Phys. Rep.* **464**, 113 (2008).

[12] N. Van Giai, B.V. Carlson, Z. Ma, H. Wolter, «The Dirac–Brueckner–Hartree–Fock approach: from infinite matter to effective Lagrangians for finite systems», *J. Phys. G: Nucl. Part. Phys.* **37**, 064043 (2010).

[13] E.N.E. van Dalen, H. Müther, «Relativistic Effects in Nuclear Matter and Nuclei», *Int. J. Mod. Phys. E* **19**, 2077 (2010).

[14] V. Rodin, «Neutron skin and giant resonances in nuclei», *Prog. Part. Nucl. Phys.* **59**, 268 (2007).

[15] K. Sharma Bharat, Subrata Pal, «Nuclear symmetry energy effects in finite nuclei and neutron star», *Phys. Lett. B* **682**, 23 (2009).

[16] K.S.A. Hassaneen, «The Equation of State of Nuclear Matter and Neutron Stars Properties», *J. Mod. Phys.* **05**, 1713 (2014).

[17] K.S.A. Hassaneen, «Asymmetric nuclear matter and neutron star properties within the extended Brueckner theory», *Eur. Phys. J. A* **53**, 9 (2017).

[18] H.M. Abou-Elsebaa, E.M. Darwish, Kh.S.A. Hassaneen, «The Effect of Various Three-Body Forces on Nuclear Matter and Neutron Stars Properties», *Moscow Univ. Phys.* **75**, 320 (2020).

[19] B.D. Day, «Elements of the Brueckner–Goldstone Theory of Nuclear Matter», *Rev. Mod. Phys.* **39**, 719 (1967).

[20] J. Hüfner, C. Mahaux, «Low density expansion of the nucleon–nucleus optical-model potential», *Ann. Phys. (N.Y.)* **73**, 525 (1972).

[21] J.P. Jeukenne, A. Lejeune, C. Mahaux, «Many-body theory of nuclear matter», *Phys. Rep.* **25**, 83 (1976).

[22] B.D. Day, «Nuclear Saturation from Two-Nucleon Potentials», *Phys. Rev. Lett.* **47**, 226 (1981).

[23] J. Carlson, V.R. Pandharipande, R.B. Wiringa, «Three-nucleon interaction in 3-, 4- and ∞-body systems», *Nucl. Phys. A* **401**, 59 (1983).

[24] M. Baldo, A. Shaban, «Dependence of the nuclear equation of state on two-body and three-body forces», *Phys. Lett. B* **661**, 373 (2008); Private communication with Professor M. Baldo.

[25] M. Baldo, L. Ferreira, «Nuclear liquid-gas phase transition», *Phys. Rev. C* **59**, 682 (1999).

[26] K. Hebeler, A. Schwenk, «Chiral three-nucleon forces and neutron matter», *Phys. Rev. C* **82**, 014314 (2010).

[27] A. Carbone, A. Polls, A. Rios, «Symmetric nuclear matter with chiral three-nucleon forces in the self-consistent Green's functions approach», *Phys. Rev. C* **88**, 044302 (2013).

[28] H.F. Arellano, F. Isaule, A. Rios, «Di-nucleon structures in homogeneous nuclear matter based on two- and three-nucleon interactions», *Eur. Phys. J. A* **52**, 299 (2016).

[29] P. Gögelein *et al.*, «Properties of asymmetric nuclear matter in different approaches», *Phys. Rev. C* **79**, 024308 (2009).

[30] H.M.M. Mansour, Kh.S.A. Hassaneen, «The properties of nuclear matter at zero and finite temperatures», *Phys. Atom. Nuclei* **77**, 290 (2014).

[31] T.L. Ainsworth *et al.*, «Equation of state of dense nuclear matter», *Nucl. Phys. A* **464**, 740 (1987).

[32] A. Ekström *et al.*, «Optimized Chiral Nucleon–Nucleon Interaction at Next-to-Next-to-Leading Order», *Phys. Rev. Lett.* **110**, 192502 (2013).

[33] A. Nogga, P. Navrátil, B.R. Barrett, J.P. Vary, «Spectra and binding energy predictions of chiral interactions for ^{7}Li», *Phys. Rev. C* **73**, 064002 (2006).

[34] P. Navrátil *et al.*, «Structure of $A = 10$–13 Nuclei with Two- Plus Three-Nucleon Interactions from Chiral Effective Field Theory», *Phys. Rev. Lett.* **99**, 042501 (2007).

[35] D. Gazit, S. Quaglioni, P. Navrátil, «Three-Nucleon Low-Energy Constants from the Consistency of Interactions and Currents in Chiral Effective Field Theory», *Phys. Rev. Lett.* **103**, 102502 (2009); *Erratum ibid.* **122**, 029901 (2019).

[36] M. Baldo, I. Bombaci, G. Giansiracusa, U. Lombardo, «On the convergence of the hole-line expansion in nuclear matter theory», *J. Phys. G: Nucl. Part. Phys.* **16**, L263 (1990).

[37] P. Danielewicz, «Determination of the mean-field momentum-dependence using elliptic flow», *Nucl. Phys. A* **673**, 375 (2000).

[38] W. Zuo, I. Bombaci, U. Lombardo, «Three-body force effect on nuclear symmetry energy and single-particle properties of asymmetric nuclear matter», *Eur. Phys. J. A* **50**, 12 (2014).

[39] E. Schiller, H. Müther, P. Czerski, «Pauli exclusion operator and binding energy of nuclear matter», *Phys. Rev. C* **59**, 2934 (1999); *Erratum ibid.* **60**, 059901 (1999).

[40] T. Frick, Kh. Gad, H. Müther, P. Czerski, «Nuclear self-energy and realistic interactions», *Phys. Rev. C* **65**, 034321 (2002).

[41] Kh.S.A. Hassaneen, H. Müther, «Correlations and spectral functions in asymmetric nuclear matter», *Phys. Rev. C* **70**, 054308 (2004).

[42] K.S.A. Hassaneen, «Spectral functions of nuclear matter using self-consistent Green's function approach based on three-body force», *Eur. Phys. J. Plus* **133**, 484 (2018).

[43] W. Zuo *et al.*, «Isospin splitting of the nucleon mean field», *Phys. Rev. C* **72**, 014005 (2005).

[44] W. Zuo, U. Lombardo, H.J. Schulze, Z.H. Li, «Three-body force rearrangement effect on single particle properties in neutron-rich nuclear matter», *Phys. Rev. C* **74**, 014317 (2006).

[45] E.N.E. van Dalen, C. Fuchs, A. Faessler, «Effective Nucleon Masses in Symmetric and Asymmetric Nuclear Matter», *Phys. Rev. Lett.* **95**, 022302 (2005).

[46] F. Coester, S. Cohen, B. Day, C.M. Vincent, «Variation in Nuclear-Matter Binding Energies with Phase-Shift-Equivalent Two-Body Potentials», *Phys. Rev. C* **1**, 769 (1970).

[47] D. Logoteta, I. Bombaci, A. Kievsky, «Nuclear matter properties from local chiral interactions with Δ isobar intermediate states», *Phys. Rev. C* **94**, 064001 (2016).

[48] F. Sammarruca *et al.*, «Dirac–Brueckner–Hartree–Fock *versus* chiral effective field theory», *Phys. Rev. C* **86**, 054317 (2012).

[49] S. Gandolfi, A. Gezerlis, J. Carlson, «Neutron Matter from Low to High Density», *Annu. Rev. Nucl. Part. Sci.* **65**, 303 (2015).

[50] I. Bombaci, U. Lombardo, «Asymmetric nuclear matter equation of state», *Phys. Rev. C* **44**, 1892 (1991); W. Zuo, I. Bombaci, U. Lombardo, «Asymmetric nuclear matter from an extended Brueckner–Hartree–Fock approach», *Phys. Rev. C* **60**, 024605 (1999).

[51] Kh. Gad, Kh.S.A. Hassaneen, «Equation of state for neutron-rich matter with self-consistent Green function approach», *Nucl. Phys. A* **793**, 67 (2007).

[52] K. Hassaneen, K. Gad, «The Nuclear Symmetry Energy in Self-Consistent Green-Function Calculations», *J. Phys. Soc. Jpn.* **77**, 084201 (2008).

[53] P.E. Haustein, «An overview of the 1986–1987 atomic mass predictions», *At. Data Nucl. Data Tables* **39**, 185 (1988).

[54] F. Sammarruca, «The Symmetry Energy: Current Status of *Ab Initio* Predictions *vs.* Empirical Constraints», *Symmetry* **15**, 450 (2023), arXiv:2212.13304 [nucl-th].

[55] C. Drischler, V. Somà, A. Schwenk, «Microscopic calculations and energy expansions for neutron-rich matter», *Phys. Rev. C* **89**, 025806 (2014).

[56] A. Akmal, V.R. Pandharipande, D.G. Ravenhall, «Equation of state of nucleon matter and neutron star structure», *Phys. Rev. C* **58**, 1804 (1998).

[57] C. Drischler, R.J. Furnstahl, J.A. Melendez, D.R. Phillips, «How Well Do We Know the Neutron-Matter Equation of State at the Densities Inside Neutron Stars? A Bayesian Approach with Correlated Uncertainties», *Phys. Rev. Lett.* **125**, 202702 (2020).

[58] P. Danielewicz, R. Lacey, W.G. Lynch, «Determination of the Equation of State of Dense Matter», *Science* **298**, 1592 (2002).

[59] M. Prakash, T.L. Ainsworth, J.M. Lattimer, «Equation of State and the Maximum Mass of Neutron Stars», *Phys. Rev. Lett.* **61**, 2518 (1988).

[60] J.R. Stone, N.J. Stone, S.A. Moszkowski, «Incompressibility in finite nuclei and nuclear matter», *Phys. Rev. C* **89**, 044316 (2014).

[61] J.-B. Wei *et al.*, «Are nuclear matter properties correlated to neutron star observables?», *Eur. Phys. J. A* **56**, 63 (2020) and references therein.